Numerical simulation of bubble growth in film boiling using a coupled level-set and volume-of-fluid method

G. Tomar and G. Biswas
Department of Mechanical Engineering, Indian Institute of Technology, Kanpur-208016, India

A. Sharma
Department of Chemical Engineering, Indian Institute of Technology, Kanpur-208016, India

A. Agrawal
Department of Mechanical Engineering, Massachusetts Institute of Technology, Cambridge, Massachusetts 02139

(Received 2 May 2005; accepted 13 October 2005; published online 23 November 2005)

A coupled level-set and volume-of-fluid method is presented for modeling incompressible two-phase flows with surface tension. The coupled algorithm conserves mass and captures the complicated interfaces very accurately. A planar simulation of bubble growth is performed in water at near critical pressure for different degrees of superheat. The effect of superheat on the frequency of bubble formation has been analyzed. In addition, simulation of film boiling and bubble formation is performed in refrigerant R134a at near critical and far critical pressures. The effect of saturation pressure on the frequency of bubble formation has also been studied. A deviation from the periodic bubble release is observed in the case of superheat beyond 15 K in water. The effect of heat flux on the instability has also been analyzed. It is found that for water at near critical condition, a decrease in superheat from 15 to 10 K leads to oscillations with subharmonics influencing the time period of the ebullition cycle. © *2005 American Institute of Physics*. [DOI: 10.1063/1.2136357]

I. INTRODUCTION

Boiling is a field that has been under extensive study in the past and has enormous applications in industry and space missions. Boiling involves extremely small spatial scales and small time constants, which make precise and extensive experimental studies rather limited. Therefore, in the past two decades, researchers started looking for solutions using computational methods, which provide solutions for fluid flow with moving interfaces separating liquid and gas phases. Remarkable developments have taken place in the past few years with regard to various numerical schemes that incorporate interface capturing or interface tracking. Many of them are based on a method called the volume-of-fluid (VOF) method, suggested by Hirt and Nichols.[1] The VOF method has been extensively used to simulate flows that have free interfaces. It uses an Eulerian approach to solve for both phases separated by a common interface. The grid is fixed and the interface is approximated within each cell through which it passes. Interface in a computational grid cell can be effectively approximated by either horizontal or vertical lines, as was pioneered by Noh and Woodward[2] in their simplified line interface calculation (SLIC) method. The line at a slope (PLIC due to Youngs[3] and LVIRA due to Puckett *et al.*[4]) or any other polynomial (PROST due to Renardy and Renardy[5]) in the grid cell is also quite successful in interface tracking. A popular interface-capturing method, known as the level-set (LS) method, was first introduced by Osher and Sethian[6] and is capable of computing geometrical properties of highly complicated boundaries without explicitly tracking the interface. In this method, the boundary of a two-fluid interface is modeled as the zero set of a smooth function ϕ defined on the entire physical domain. The boundary is then updated by solving a nonlinear equation of the Hamilton-Jacobi type on the whole domain. The LS method captures the interface very accurately, however it may lead to violation of mass conservation if improperly implemented. LS function must be advected with a proper extension-velocity field, defined throughout the domain such that it matches with the true velocity field at the zero level set and also moves the neighboring level sets in a way that the signed distance function is preserved. Using this approach, reinitialization of the LS need not be done every time step (cf. Sethian[7]). Another approach to achieve mass conservation is to couple the level-set methodology with the VOF method. The coupled level-set and volume-of-fluid (CLSVOF) method was introduced by Bourlioux[8] and further developed by Sussman and Puckett.[9] In the CLSVOF method, the level set is used only to compute the geometric properties (normal and curvature) at the interface while void fraction is advected using the VOF approach. Sussman[10] demonstrated the capability of the method for analyzing and computing the growth and collapse of vapor bubbles.

The most widely used model for horizontal film boiling is the one suggested by Berenson,[11] which is based on a linear stability analysis assuming only gravity and surface tension playing major roles in instabilities leading to bubble formation. The "most dangerous" Taylor wavelength is given by

$$\lambda_0 = 2\pi\sqrt{\frac{3\sigma}{(\rho_l - \rho_g)g}}. \quad (1)$$

The above-mentioned relation assumes that the effects of vapor velocity and film thickness on the liquid-vapor boundary layer are negligible. Thus, by solving the equations under the creeping flow approximation in the momentum equation, coupled with the assumption that convective energy transport is negligible in the film, Berenson[11] gave an expression for the Nusselt number as

$$\mathrm{Nu} = 0.425\left(\frac{\rho_g(\rho_l - \rho_g)gh_{lg}}{k_g\mu_g\Delta\theta}\right)^{1/4}(\lambda)^{3/4}, \quad (2)$$

where λ, the characteristic length, is given by

$$\lambda = \sqrt{\frac{\sigma}{(\rho_l - \rho_g)g}}. \quad (3)$$

Berenson's correlation shows good agreement with the experimental data. It assumes that the wall superheat is spatially uniform and time invariant.

Simulation of boiling, without considering the major assumptions stated in Berenson's simplified model, started with the work of Son and Dhir,[12] who used the Lagrangian approach to track the interface. A moving mesh technique was used to discretize the vapor and liquid zones. Separate sets of equations were considered and the mesh was reconstructed after each time step. Using the same method, Banerjee and Dhir[13] simulated subcooled film boiling. In both cases, the evolution of the bubble was followed only until the bubble detachment. Later, Juric and Tryggvason[14] used the Eulerian grid to simulate horizontal film boiling, using source terms in the continuity equation. The source term accounted for the interfacial mass transfer due to phase change. Using a similar approach, Son and Dhir[15] simulated axisymmetric horizontal film boiling. Uniform wall superheat boundary conditions were used to simulate boiling of water at near critical condition. They could predict steady-state periodic release of bubbles, which was also witnessed in experiments (Reimann and Grigull[16]). Welch and Wilson[17] modified the VOF method of Youngs[3] and obtained a steady-state bubble release pattern using uniform wall heat flux boundary conditions. Welch and Rachidi[18] further extended this work considering a conjugate problem, which requires the solution of the fluid region in conjunction with the energy equation for a solid through which energy is transferred to the vapor. Agarwal *et al.*[19] predicted bubble growth, ebullition cycle, and transport coefficients on the horizontal surface. The simulations also highlighted the importance of variable properties.

In the present work, the CLSVOF method has been used for computing two-phase flows in film boiling. Two examples have been chosen to illustrate the power of the method in calculating the fluid flow and boiling heat transfer across the free boundary. Simulations have been performed for refrigerant R134a at near critical and far critical conditions. Also, simulations have been performed for water at a near critical point (pressure −219 bars). The effect of superheat on the periodic nature of film boiling, including formation, alternate growth, and detachment of bubble at neighboring sites, has been studied. We show that this phenomenon leads to temporal oscillations of the space-averaged Nusselt number. The fast Fourier transform (FFT) analysis quantifies the effect of superheat on frequency of oscillations. A simple model based on lubrication approximation (Panzarella *et al.*[20]) has been used here to study the bivalent characteristics of heat flux during the initial phase of bubble growth in film boiling.

II. FORMULATION

A. Governing equations

The momentum transport equation for incompressible flow in the single-phase regions (i.e., either the vapor or the liquid) is

$$\rho(\mathbf{U}_t + \nabla\cdot\mathbf{UU}) = -\nabla p + \rho\mathbf{g} + \nabla\cdot(2\mu\mathbf{D}) \quad (4)$$

and at the interface the modified momentum equation incorporating surface tension force due to Brackbill *et al.*[21] becomes

$$\rho(\mathbf{U}_t + \nabla\cdot\mathbf{UU}) = -\nabla p + \rho\mathbf{g} + \nabla\cdot(2\mu\mathbf{D}) + \sigma\kappa\mathbf{n}\delta_s, \quad (5)$$

where $\mathbf{n}$ is the unit normal vector at the interface, κ is the curvature of the interface, δ_s is the surface delta function, and $\mathbf{D}$ is defined as the rate of deformation tensor,

$$\mathbf{D} = \tfrac{1}{2}\{(\nabla\mathbf{U}) + (\nabla\mathbf{U})^T\}. \quad (6)$$

The mass conservation equation for the incompressible flow in the single-phase region is

$$\nabla\cdot\mathbf{U} = 0. \quad (7)$$

The method used to solve for velocity and pressure is a variable density approximate projection method described in Puckett *et al.*[4]

The energy equation in the single-phase regions is given by

$$\frac{\partial T}{\partial t} + \mathbf{U}\cdot\nabla T = \frac{k}{\rho c}\nabla^2 T. \quad (8)$$

However, both the mass conservation equation (7) and the energy equation (8) need to be modified at the interface that involves the interfacial mass and energy transfer.

B. Mass and energy jump conditions

Due to phase change at the interface, there is a jump in the mass and energy across the interface. Considering a computational two-phase cell (Fig. 1) with a part of the interface, the mass balance equation for each phase in the cell can be written as

$$\frac{d}{dt}\int_{V_g(t)}\rho dV + \int_{S_g(t)}\rho\mathbf{U}\cdot\mathbf{n}dS + \int_{S_I(t)}\rho(\mathbf{U}-\mathbf{U}_I)\cdot\mathbf{n}dS = 0, \quad (9)$$

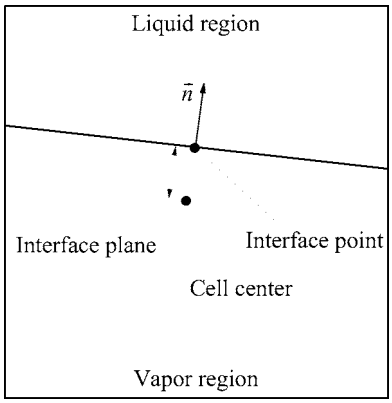

FIG. 1. Definition of the piecewise-linear interface.

$$\frac{d}{dt}\int_{V_l(t)} \rho dV + \int_{S_l(t)} \rho \mathbf{U}\cdot\mathbf{n}dS + \int_{S_I(t)} \rho(\mathbf{U}-\mathbf{U}_I)\cdot\mathbf{n}dS = 0, \tag{10}$$

where $V_l(t)$, $S_l(t)$, $V_g(t)$, and $S_g(t)$ are the volumes and surface area of the cell boundary at the liquid region and the vapor region, respectively. $S_I(t)$ is the phase interface at the common boundary of the two regions moving with velocity U_I. The unit normal vector $\mathbf{n}$ points into the liquid phase on S_I.

From Eqs. (9) and (10) and taking into account the incompressibility of each phase, and that the total volume of the cell remains time-invariant, the conservation of mass equation for the cell is given by

$$\int_{S_C} \mathbf{U}\cdot\mathbf{n}dS + \int_{S_I(t)} \|(\mathbf{U}-\mathbf{U}_I)\|\cdot\mathbf{n}dS = 0. \tag{11}$$

Here $\|.\|$ indicates the jump in the variable across the interface and S_C is the boundary of the computational cell. The mass jump condition at the interface is

$$\|\rho(\mathbf{U}-\mathbf{U}_I)\|\cdot\mathbf{n} = 0. \tag{12}$$

Similarly, the energy jump condition is

$$\|\rho h_{lg}(\mathbf{U}-\mathbf{U}_I)\|\cdot\mathbf{n} = -|\mathbf{q}|\cdot\mathbf{n}, \tag{13}$$

where $\mathbf{q}$ is the heat flux vector at the interface and h_{lg} is the enthalpy. From (12) and (13), the jump in the conservation of mass equation becomes

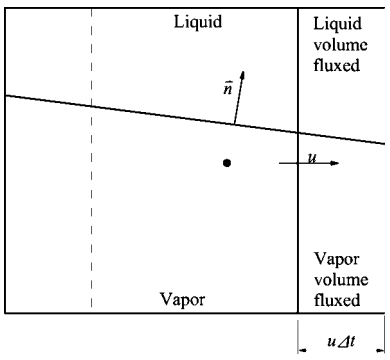

FIG. 2. Calculation of the fluxed void fraction at the right cell face.

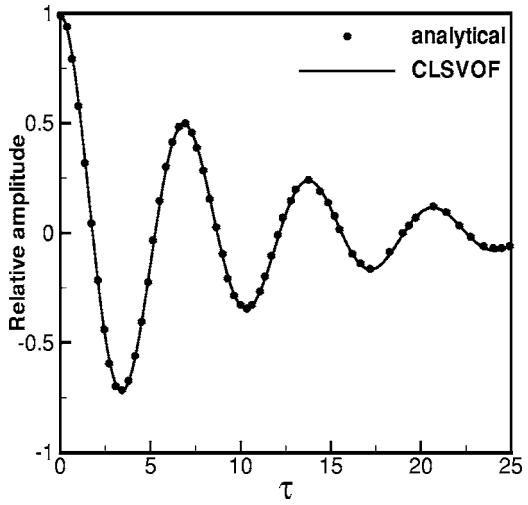

FIG. 3. Relative amplitude of the capillary wave for the viscous case. Results obtained using CLSVOF are compared with the analytical solution of Prosperitti (Ref. 26).

$$\|(\mathbf{U}-\mathbf{U}_I)\|\cdot\mathbf{n} = \left(\frac{1}{\rho_l}-\frac{1}{\rho_g}\right)\frac{|q|\cdot\mathbf{n}}{h_{lg}}. \tag{14}$$

Using (11) and (14) we have the continuity equation at the interface as

$$\int_{S_C} \mathbf{U}\cdot\mathbf{n}dS + \int_{S_I(t)} \left(\frac{1}{\rho_l}-\frac{1}{\rho_g}\right)\frac{|q|\cdot\mathbf{n}}{h_{lg}}dS = 0. \tag{15}$$

C. Interface tracking using the level-set function

In the LS method, a smooth function ϕ is used to represent the interface. The function $\phi(\mathbf{r},t)$ at a point with position vector $\mathbf{r}$ and at a time instant t assumes values as the following:

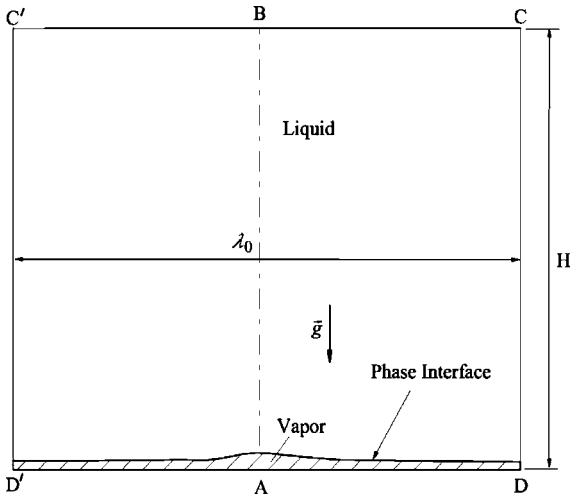

FIG. 4. Computational domain. ABCD represents the computational domain chosen for simulations. "A" is the node (bubble nucleation site) and "D, D′" are antinodes. Shaded region represents vapor under the liquid.

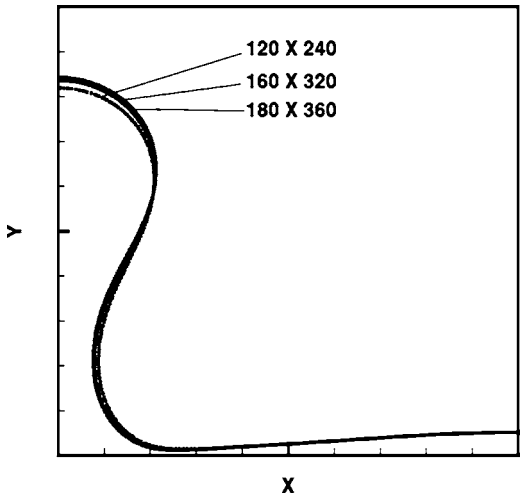

FIG. 5. Bubble interface profile for three different grid resolutions.

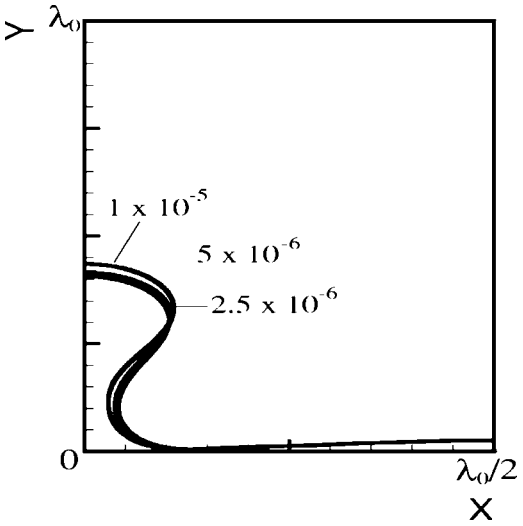

FIG. 6. Time convergence study showing bubble interface at 0.1 s for a grid mesh of 180×360 using three different time steps.

$$\phi(\mathbf{r},t)\begin{cases}<0 \text{ in the gas region},\\ =0 \text{ at the interface},\\ >0 \text{ in the liquid region}.\end{cases}$$

The level-set function chosen here is maintained as the signed distance from the interface close to the interface. Hence, near the interface,

$$\phi(\mathbf{r},t)\begin{cases}=-d \text{ in the gas region},\\ =0 \text{ at the interface},\\ =+d \text{ in the liquid region},\end{cases}$$

where $d=d(t)$ is the shortest distance of the interface from point $\mathbf{r}$. From such a representation of the interface, the unit normal vector $\mathbf{n}$ and the mean curvature κ are simply

$$\mathbf{n}=\frac{\nabla\phi}{|\nabla\phi|} \tag{16}$$

and

$$\kappa=-\nabla\cdot\frac{\nabla\phi}{|\nabla\phi|}. \tag{17}$$

D. Modified equations

Using the level-set formulation due to Chang *et al.*,[22] the momentum transport equation for incompressible two-phase flow becomes

$$\rho(\phi)(\mathbf{U}_t+\nabla\cdot\mathbf{UU})=-\nabla p+\rho(\phi)\mathbf{g}+\nabla\cdot[2\mu(\phi)\mathbf{D}]+\sigma\kappa(\phi)\,\nabla\mathbf{H}(\phi) \tag{18}$$

and the LS function advection equation is

$$\frac{\partial\phi}{\partial t}+\mathbf{U}\cdot\nabla\phi=0. \tag{19}$$

The density and viscosity are derived from the level-set function as

$$\rho(\phi)=\rho_g[1-H(\phi)]+\rho_l H(\phi), \tag{20}$$

$$\mu(\phi)=\mu_g[1-H(\phi)]+\mu_l H(\phi), \tag{21}$$

where $H(\phi)$ is the Heaviside function,

$$H(\phi)=\begin{cases}0 & \text{if } \phi<-\epsilon,\\ \dfrac{1}{2}+\dfrac{\phi}{2\epsilon}+\dfrac{1}{2\pi}\left[\sin\left(\dfrac{\pi\phi}{\epsilon}\right)\right].\end{cases} \tag{22}$$

The local mean curvature is given by Eq. (17).

When discretizing the LS advection equation (19), the volume-of-fluid function α is also simultaneously solved from the following equation:

$$\frac{\partial\alpha}{\partial t}+\nabla\cdot(\mathbf{U}\alpha)=0. \tag{23}$$

III. NUMERICAL METHODS AND DISCRETIZATION

A. Discretization of momentum and continuity equation

The momentum equation (18) is discretized in time as

TABLE I. Properties of liquid and vapor phases of water at near critical pressure (P_r=0.99).

Water near critical: T_{sat}=646 K; P_{sat}=21.9 MPa; h_{lg}=276.4 kJ/kg; σ=0.07 mN/m

	Density (ρ) (kg/m^3)	Viscosity (μ) (μN s/m^2)	Conductivity (K) (mW/mK)	Specific heat (c_p) (kJ/kg K)
Liquid	402.4	46.7	545	2.18×10^2
Vapor	242.7	32.38	538	3.52×10^2

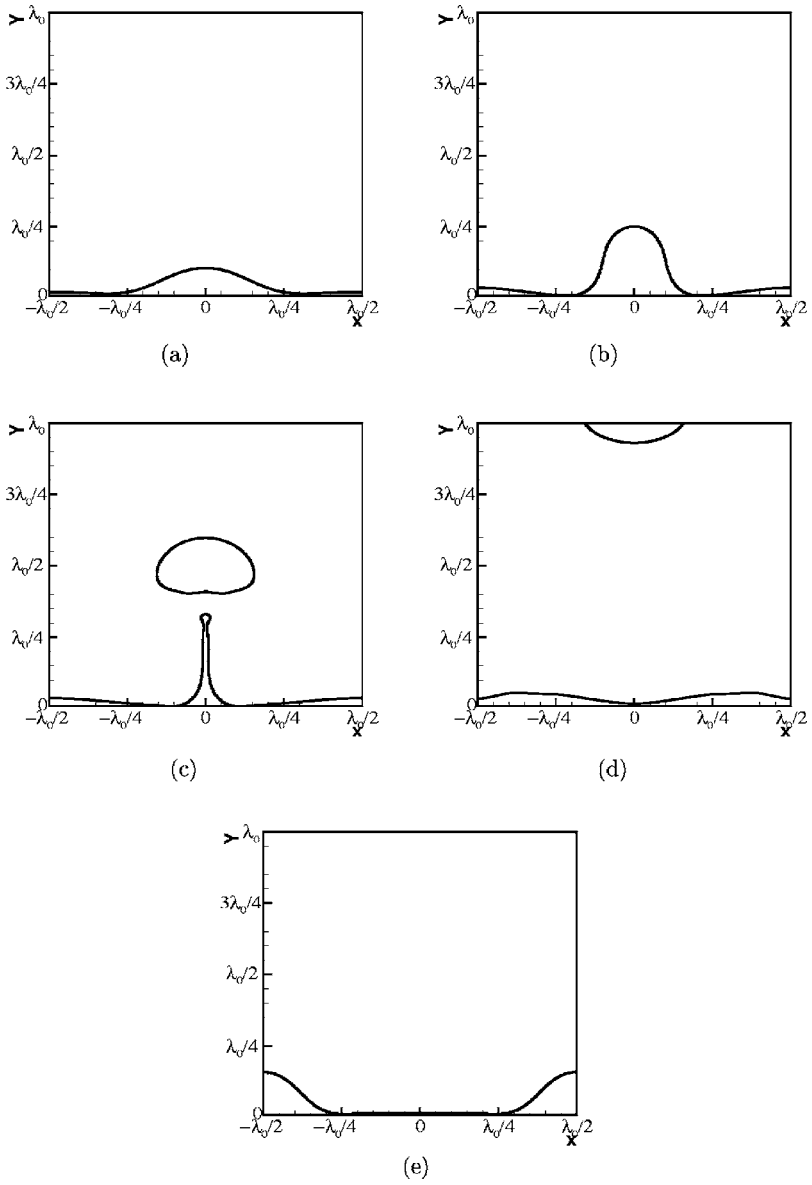

FIG. 7. Interface morphology at different instants of a bubble release cycle for water ($P_r=0.99$) with $\Delta T_{\text{sup}}=10$ K.

$$\mathbf{U}^{n+1}=\mathbf{U}^n+\left(-\nabla\cdot(\mathbf{U}^n\mathbf{U}^n)+\mathbf{g}+\frac{[-\nabla p^{n+1}+\nabla\cdot 2\mu\ (\phi^n)\mathbf{D}^{\mathbf{n}}]+\sigma\kappa(\phi^n)\nabla H(\phi^n)}{\rho(\phi^n)}\right)\delta t. \tag{24}$$

The convection term of Eq. (24) is discretized using a high-order upwind ENO scheme as described in Puckett *et al.*[4] The continuity equations in the single-phase regions (7) and at the interface (15) are, respectively, discretized in time,

$$\nabla\cdot\mathbf{U}^{n+1}=0 \tag{25}$$

and

$$\int_{S_c}\mathbf{U}^{n+1}\cdot\mathbf{n}dS+\int_{S_l(t)}\left(\frac{1}{\rho_l}-\frac{1}{\rho_g}\right)\frac{\|\mathbf{q}^{n+1}\|\cdot\mathbf{n}}{h_{l_g}}\cdot\mathbf{n}dS=0. \tag{26}$$

For solving the pressure, the pressure correction is done using a variable density approximate projection method described in Puckett.[4]

B. Discretization of the energy equation

In the vapor region, the energy equation (8) is solved using an implicit scheme,

$$T^{n+1}=T^n+\left(-\mathbf{U}\cdot\nabla T^{n+1}+\frac{k}{\rho c}\nabla^2 T^{n+1}\right)\delta t. \tag{27}$$

However, in the liquid region and at the interface, the temperature is taken to be constant at the saturation temperature. Hence, in the liquid region and at the interface,

$$T=T_{\text{sat}}. \tag{28}$$

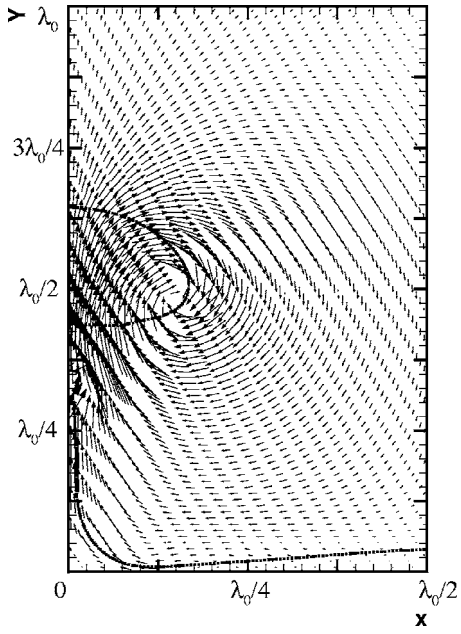

FIG. 8. Velocity vectors for a superheat of $\Delta T_{sup}=10$ K (water) just after a bubble release.

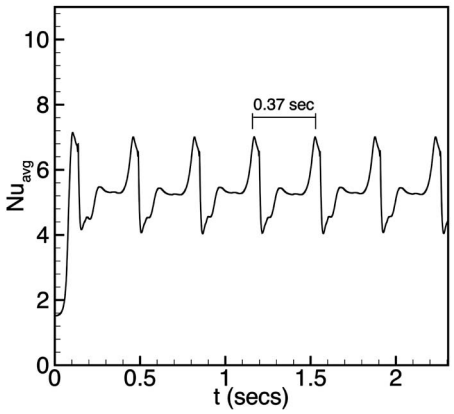

FIG. 9. Space-averaged Nusselt number variation with time for water at near critical pressure with $\Delta T_{sup}=10$ K.

C. The CLSVOF advection algorithm

A coupled second-order conservative operator split advection scheme was used for discretization of Eqs. (19) and (23) as described in Rudman.[23] This is done in three steps, as follows.

(1) The LS function and void fraction are fluxed across the cell boundaries in one direction (say the x direction) as shown in Fig. 2.
(2) The interface is reconstructed using the newly obtained void fraction field and LS function.
(3) The LS function and void fraction are fluxed across the cell boundaries in the other direction (say the y direction).

The flux directions are swapped after every time iteration.

At each time step after finding the updated level set function ϕ^{n+1} and the volume-of-fluid function, α^{n+1}, the level-set function is reinitialized to the exact signed normal distance from the reconstructed interface by coupling the level-set function to the volume fraction (Sussman *et al.*[9]).

D. Calculation of curvature

The normal is given by Eq. (16),

$$\mathbf{n}=\frac{\phi_x\mathbf{i}+\phi_y\mathbf{j}}{\sqrt{\phi_x^2+\phi_y^2}}, \tag{29}$$

where $\mathbf{i}$ and $\mathbf{j}$ are the unit vectors along the two orthogonal reference axes. The curvature in Eq. (17) is given by

$$\kappa=-\left(\frac{\phi_y^2\phi_{xx}-2\phi_x\phi_y\phi_{xy}+\phi_x^2\phi_{yy}}{(\phi_x^2+\phi_y^2)^{3/2}}\right). \tag{30}$$

The present algorithm has been tested extensively[24] to verify its accuracy to predict the results of a host of benchmark problems. A test to rigorously check the mass-conserving and proper advection capability of an interface tracking method is that of a circle in a shear flow. A circle is placed in a divergence-free shear velocity. The interfaces computed after 1000 time steps forward and 1000 time steps backward (velocity direction reversed) result in a mass loss of less than 10^{-4} in the circle. Another test known as the capillary wave test described in Popinet and Zaleski[25] is used to test the surface tension computation of a two-phase flow computation algorithm. A square box is divided into two equal parts by a sinusoidal perturbation. The width of the box is chosen as $\lambda=H=3$, where λ and K are the wavelength and the wave number, respectively. The boundary condition at the top and the bottom wall is that of free slip. Periodic boundary conditions are imposed along the horizontal axis. The amplitude of the perturbation is 0.01λ. The Ohnesorg number $[\mathrm{Oh}=\mu/(\rho\sigma\lambda)^{1/2}]$ is chosen as $1/\sqrt{3000}$. The nondimensional viscosity $[\epsilon=\mu K^2/(\rho\omega_0)]$ is 6.472×10^{-2}, where ω_0 is the growth coefficient given by the dispersion relation $\omega_0^2=\sigma K^2/2\rho$. Figure 3 shows the decay of the amplitude relative to the initial perturbation $[0.01\lambda\cos(2\pi x/\lambda)]$ with time. The computed amplitude closely follows the analytical results of Prosperetti.[26] The relative error using CLSVOF (64^2 grid mesh) is around 3×10^{-3} compared to 9.8×10^{-3} of Popinet and Zaleski.[25]

The computational domain chosen for the present simulations is shown in Fig. 4. The height of the domain, H, was set as λ_0. The initial interface height δ was set to

$$\delta=\frac{\lambda_0}{64}\left(4+\cos\frac{(2\pi x)}{\lambda_0}\right). \tag{31}$$

The initial film thickness is maximum at "$x=0$" defined as the node and minimum at "$x=\lambda_0/2$" defined as the antinode. Only half the wavelength, i.e., node to antinode, is taken along the x axis for computations. The domain height along the y axis is twice the domain width along the x axis. The boundary conditions on both the left face and the right face of the domain are symmetry boundary conditions,

$$\text{at } x=0: \quad u=0,\ \frac{\partial v}{\partial x}=0,\ \frac{\partial T}{\partial x}=0,\ \frac{\partial \alpha}{\partial x}=0,\ \frac{\partial \phi}{\partial x}=0,$$

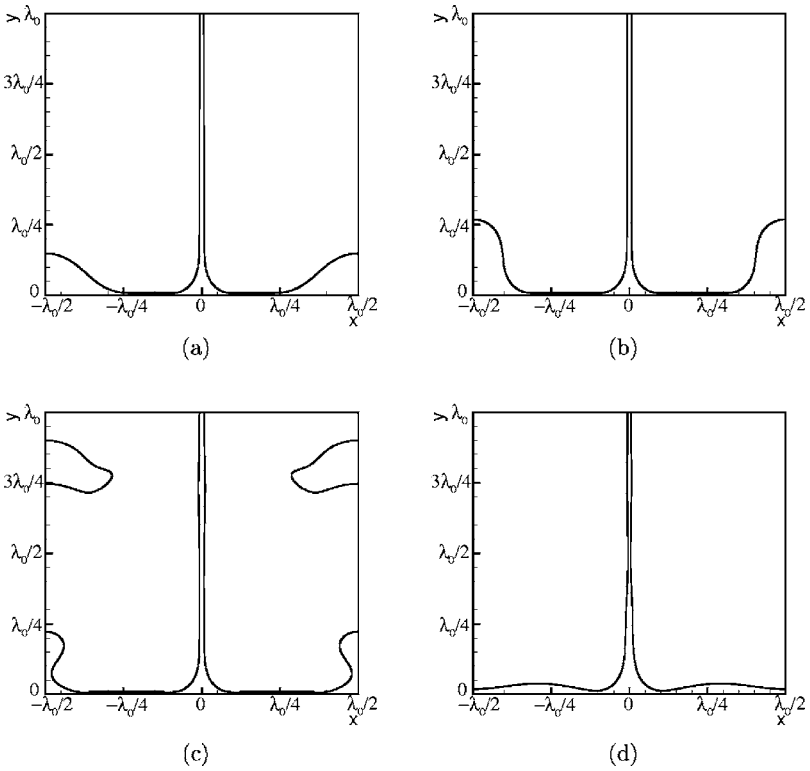

FIG. 10. Vapor jet column formation for a superheat of 17 K in water at near critical pressure.

$$\text{at } x = \lambda/2: \quad u = 0,\ \frac{\partial v}{\partial x} = 0,\ \frac{\partial T}{\partial x} = 0,\ \frac{\partial \alpha}{\partial x} = 0,\ \frac{\partial \phi}{\partial x} = 0.$$

Outflow boundary conditions are used on the top surface of the domain,

$$\text{at } y = H: \quad \frac{\partial u}{\partial y} = \frac{\partial v}{\partial y} = \frac{\partial T}{\partial y} = \frac{\partial \alpha}{\partial y} = \frac{\partial \phi}{\partial y} = 0;\ P = P_0.$$

The outlet pressure is taken to be the saturation pressure less than the hydrostatic pressure difference from the initial film level to the outlet. At the bottom wall, for the constant wall temperature model,

$$\text{at } y = 0: \quad T = T_{\text{sat}} + \Delta T_{\text{sup}}.$$

A grid independence test was performed using 120×240, 160×320, and 180×360 grid meshes. Figure 5 shows the difference between profiles obtained after 19 500 time steps ($\Delta t = 5 \times 10^{-6}$). The maximum relative difference in height of the profiles obtained for 120×240 and 160×320 meshes is around 2%, while for 160×320 and 180×360 meshes it is 0.7%. In this study, a 180×360 grid mesh has been used for simulations.

During the computations, time steps were chosen to satisfy the CFL condition and the capillary time condition. An appropriate time step ($\Delta t = 5 \times 10^{-6}$), which satisfies the above conditions, has been used for all the cases. Figure 6 shows the profiles for different time steps obtained at $t = 0.1$ s. The maximum relative difference in height of the profiles obtained for $\Delta t = 1 \times 10^{-5}$ and $\Delta t = 5 \times 10^{-6}$ is 4%, while for $\Delta t = 5 \times 10^{-6}$ and $\Delta t = 2.5 \times 10^{-6}$ it is 2%. In this study, a time step of $\Delta t = 5 \times 10^{-6}$ has been used. It took around 758 min to compute two consecutive bubble detachments (water at near critical pressure $\Delta T_{\text{sup}} = 10$ K, 180×360 grid mesh, $\Delta t = 5 \times 10^{-6}$) using a Pentium IV, 3.6 GHz HT processor having 2 GB RAM.

Results and discussions in the present work have been organized around the following test cases:

(A) Simulations for water at near critical pressure ($P_r = 0.99$).
(B) Simulations for R134a at near critical ($P_r = 0.92$) and far critical pressure ($P_r = 0.12$). With the above test cases, the following aspects have been studied in detail:
(C) Behavior of the Nusselt number.
(D) Effect of heat flux on instability.

IV. RESULTS AND DISCUSSIONS

A. Simulations for water at near critical pressure

The properties given in Table I are used for the liquid and vapor phases of water at the near critical conditions. The periodic bubble release patterns with growing interface are shown in Figs. 7(a)–7(e). The velocity vector plot (Fig. 8)

TABLE II. Properties of liquid and vapor phases of refrigerant R134a at near critical pressure ($P_r = 0.92$).

R134a near critical: $T_{\text{sat}} = 370.46$ K; $P_{\text{sat}} = 3.763$ MPa; $h_{lg} = 54.6$ kJ/kg; $\sigma = 0.182$ mN/m				
	Density (ρ) (kg/m^3)	Viscosity (μ) (μN s/m^2)	Conductivity (K) (mW/mK)	Specific heat (c_p) (kJ/kg K)
Liquid	730.8	56.72	52	5.128
Vapor	301.9	21.71	41.5	4.445

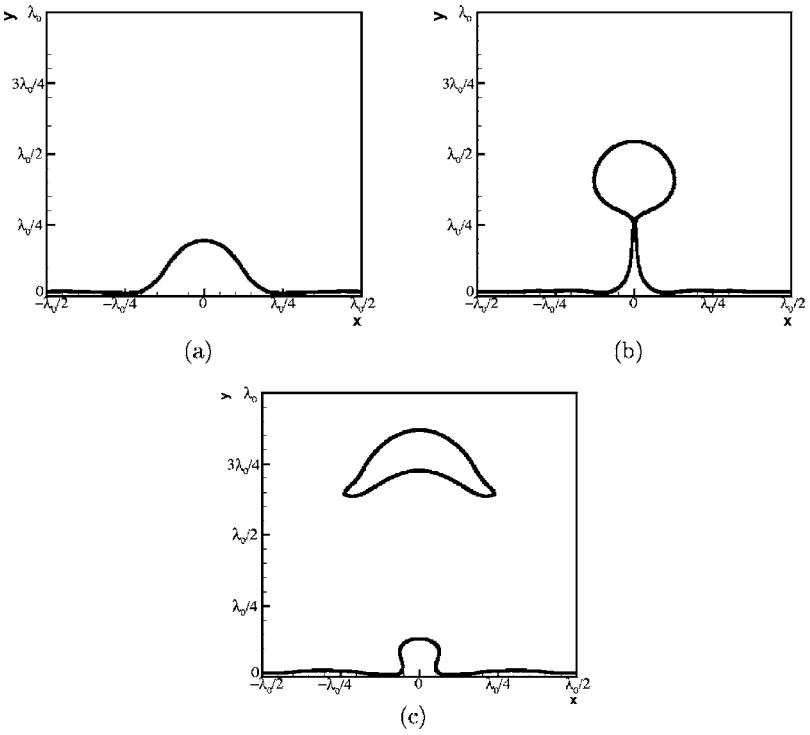

FIG. 11. Interface morphology at different instants of a bubble release cycle for R134a (P_r=0.92) with ΔT_{sup} =30 K.

shows high velocity gradients near the detachment point as the liquid from the bulk is rushed into the gap between the detached bubble and the film. Velocity is small in most of the film away from the bubble. At the points surrounding the slender vapor column, where film thickness is minimal, vapor production is maximal and vapor produced in this zone has a velocity toward the node even after detachment of the bubble has taken place. Due to the formation of a wake behind the rising bubble, the bottom interface of the bubble is pushed up, leading to the formation of an inverted cup. The bubble becomes increasingly spherical due to surface tension as it rises up. The vapor column is pulled back due to capillary forces. The disturbance travels toward the antinode and leads to bubble growth at the antinode. This cycle repeats periodically and bubble formation occurs alternatively at the node and the antinode. Space-averaged Nusselt number distribution over time is shown in Fig. 9. The four dynamically distinct periodic regimes in Fig. 9 are discussed later in Sec. IV C. The computed time- and space-averaged Nusselt number from Fig. 6 is found to be 5.37. The time- and space-averaged Nusselt number for a similar physical situation, as predicted by Berenson's correlation, is 4.297, which is around 20% smaller.

The frequency of bubble detachment, using temporal variation of the Nusselt number, is found to be one bubble in 0.37 s. Simulations were also performed with a superheat of 15 and 17 K and a notable change in bubble dynamics took place between superheats of 15 and 17 K. For a superheat of 15 K, the interface profile similar to 10 K was obtained and the bubble detachment also took place alternatively from node and antinode (not shown in the figure). But for 17 K superheat, a very tall and slender vapor column formation was observed as shown in Fig. 10. The columnar jet remains stable and the periodic bubble formation now always occurs at the antinodes. Similar profiles were observed in the experiments of Reimann and Grigull,[16] in which higher values of heat flux beyond a critical value were used. It was observed that after a critical value of heat flux, this change in bubble dynamics and interface structure takes place. Using an axisymmetric formulation, Son and Dhir[15] observed the formation of vapor columns in their simulations.

This phenomenon of stable vapor column formation is observed at near critical pressures for even moderate superheats. Such vapor columns can disintegrate into fragments, because they are subject to Kelvin-Helmoltz instability, as there is a relative velocity between the vapor and the liquid. Analysis of such columns and condition on superheat for

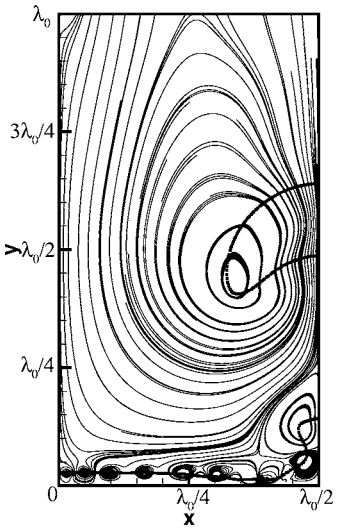

FIG. 12. Streamlines showing vortex formations at locations of high curvature [R134a (P_r=0.92) with ΔT_{sup}=30 K].

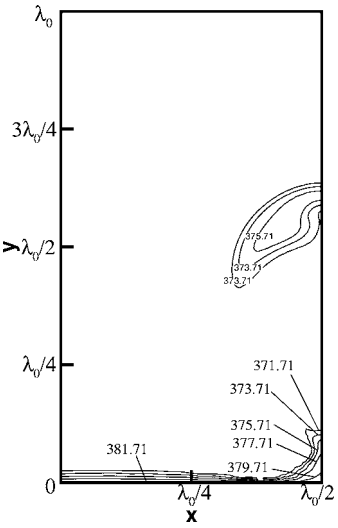

FIG. 13. Isotherms for R134a (P_r=0.92) with ΔT_{sup}=30 K at an instant when the vapor column has collapsed.

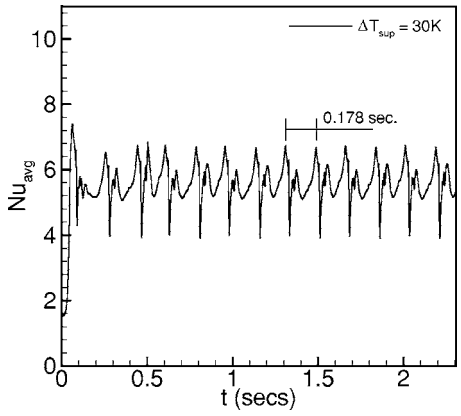

FIG. 14. Space-averaged Nusselt number variation with time for R134a (P_r=0.92) with ΔT_{sup}=30 K.

stability of vapor columns is given in Son and Dhir.[15] The analysis was done for cylindrical vapor jets in liquid and an expression for critical vapor velocity was given. Following the model of Son and Dhir, the minimum superheat required to maintain the stable columns in the case of present simulation is found to be 6.7 K. Since the formation of such tall slender vapor columns occurs at only high values of superheat, the vapor columns thus formed are stable and do not break into fragments.

B. Simulations for R134a at near critical and far critical pressure

The data in Table II are used for the liquid and vapor phase of R134a at the near critical condition. Bubble profiles at various time instants are shown in Figs. 11(a)–11(c). The film grows forming a bubble that detaches, leaving a slender vapor column of height close to $\lambda_0/4$. The column collapses and the rising bubble forms an inverted cup that later becomes increasingly spherical as the bubble buoys away. The disturbance in the remaining film now travels toward the antinode and the cycle repeats at the antinode. The streamlines (Fig. 12) depict the formation of a vortex at locations of high curvatures. Superheat used for the simulation is 30 K. From the temperature contours in Fig. 13, it is clear that the isotherms almost follow the shape of the interface. The spacing between isotherms is in general uniform, as also observed in Agarwal *et al.*[19]

The space-averaged Nusselt number obtained by simulations is shown in Fig. 14. The time- and space-averaged Nusselt number computed using Berenson's correlation for this case is 4.77, as compared to 5.615 obtained through computations, showing a variation of −15.05%. The frequency of bubble detachment is found to be one bubble in 0.178 s. The time period is smaller than that for water at near critical condition. Simulations were also performed with superheats of 10 and 50 K. A short time view of fluctuations in the Nusselt number is shown in Fig. 15 for different degrees of superheat. At a superheat of 10 K, there are modulations in the Nusselt number distribution reflecting stronger instability of thinner vapor film at lower superheats. The frequency of bubble detachment is high (one bubble in 0.12 s) for 50 K superheat value. Figure 15 shows a comparison of Nusselt numbers for the superheat of 10, 30, and 50 K.

Simulations at a pressure much less than critical pressure (P_r=0.125) were also performed. The properties in Table III are used for the liquid and the vapor phase of R134a at the far critical condition. Figure 16 shows bubble profiles at different time instants. A bubble grows at the antinode, necks, and then detaches leaving a thin film. Vapor column collapse is much faster when compared to the R134a near critical case (Fig. 11). The surface tension coefficient is much larger at far critical pressures, thus the column collapse is expected to be much faster at far critical conditions. Temperature contours at the time when necking of the interface has just started are shown in Fig. 17. Isotherms are almost uniformly spaced along the interface, similar to those obtained for R134a at near critical pressure. The space-averaged Nusselt number over time is shown in Fig. 18. The high-frequency modulations are observed in the plot between bubble detachment peaks. Due to the large liquid to vapor density ratio, the system is quite susceptible to Rayleigh-Taylor instability (cf.

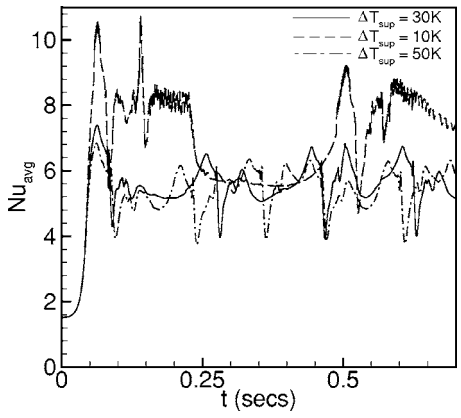

FIG. 15. A short time view of fluctuations in the Nusselt number for R134a (P_r=0.92) with ΔT_{sup}=10, 30, and 50 K.

TABLE III. Properties of liquid and vapor phases of refrigerant R134a at far critical pressure (P_r=0.125).

R134a far critical: T_{sat}=289 K; P_{sat}=0.5 MPa; h_{lg}=185.9 kJ/kg; σ=9.331 mN/m				
	Density (ρ) (kg/m^3)	Viscosity (μ) (μN s/m^2)	Conductivity (K) (mW/mK)	Specific heat (c_p) (kJ/kg K)
Liquid	1240.3	218.5	85	1.391
Vapor	24.36	11.32	12.9	0.965

p. 428 of Chandrashekhar[27]), which is suppressed by the heat flux from the bottom wall, therefore large superheat (80 K) was used for this case.

The time- and space-averaged Nusselt number obtained through computations is 7.79. Frequency of bubble detachment is found to be one bubble in 0.714 s, which is very low compared to the R134a near critical case.

C. Behavior of the Nusselt number

The Nusselt number depends strongly on the film thickness, as also observed in Agarwal *et al.*[19] Heat flux is more at the locations where the film is thin and less where the film is thick. Average heat flux, therefore, increases when more vapor rushes to fill the bubble and the remaining film becomes vapor deficient, thus reducing its thickness and leading to a higher Nusselt number. On the contrary, when the film is almost uniform, it is thick and correspond to the lowest Nusselt number value of the curve. With the growth of the instability, the interface at certain locations comes very close to the heated surface, thus resulting in an increased average spatial Nusselt number. With the growth of the instability, more and more regions become vapor-deficient and the Nusselt number keeps increasing until the interface necks and bubble detachment takes place. Thus, the first peak of the Nusselt number depicts a bubble detachment. As the bubble rises, the liquid rushes in the space between the bubble and the interface and pushes the interface downwards. The vapor column now collapses due to interfacial tension and the vapor-deficient regions receive vapors both from the shrinking column and from continued vaporization. The thickening of the interface results in the fall of the Nusselt number. Under the action of the wake behind the bubble, the interface again necks slightly, which leads to the formation of another sharp rise in the Nusselt number.

The retreating vapor makes the film unstable and fills in at the antinode. A new bubble formation now takes place at

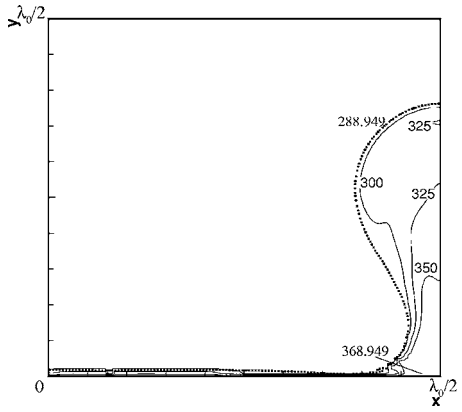

FIG. 17. Isotherms for R134a (P_r=0.12) with ΔT_{sup}=80 K at an instant when the bubble starts necking.

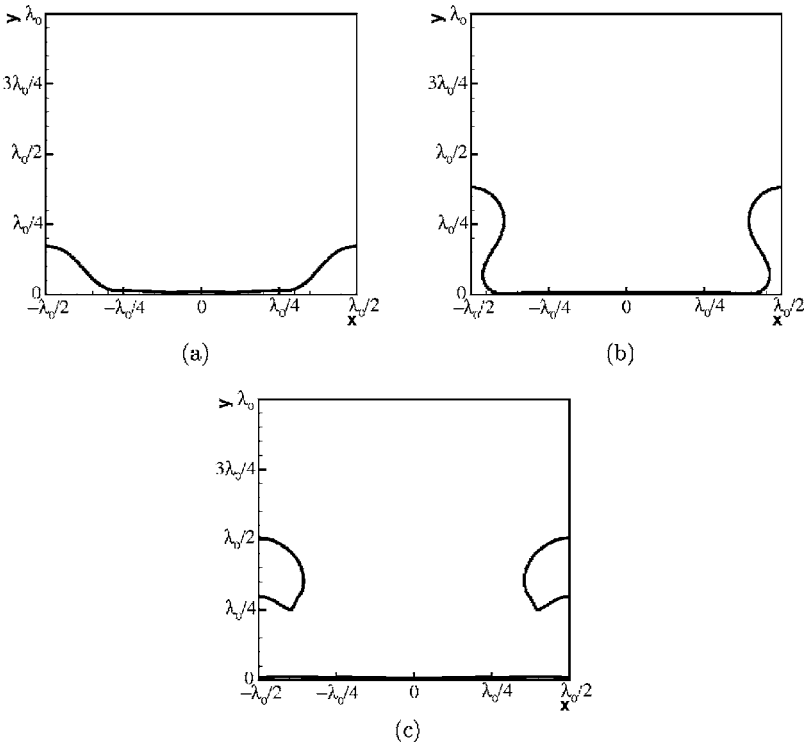

FIG. 16. Interface morphology at different instants of a bubble release cycle for R134a (P_r=0.12) with ΔT_{sup} =80 K.

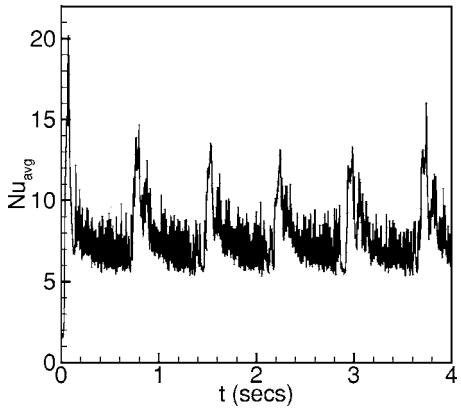

FIG. 18. Space-averaged Nusselt number variation with time for R134a (P_r=0.12) with ΔT_{sup}=80 K.

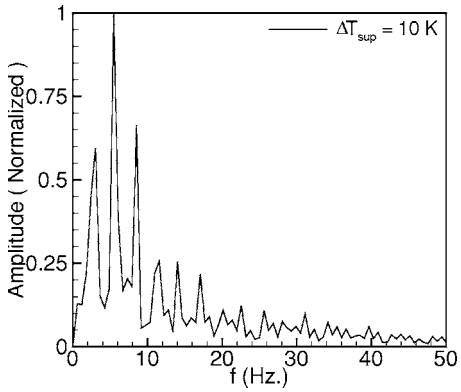

FIG. 20. Normalized FFT of Nusselt number variation with time for water (P_r=0.99) with ΔT_{sup}=10 K.

the antinode, and this cycle continues and is called the ebullition cycle. Figure 19 shows that with 17 K superheat, the space-averaged Nusselt number distribution shows single peaks. Since at the node a column is formed (Fig. 10), peaks are obtained during the bubble detachment from the antinodes only.

D. Effect of heat flux on instability

Heat flux plays a destabilizing role in evaporating thin liquid films (Burelbach *et al.*[28]). In the case of film boiling, it has bivalent characteristics. Although heat flux always favors a vapor film formation on the heating surface, it also supports the periodic departure of bubbles from the surface.

When the film is almost uniform, after the bubble detachment and the vapor column collapse, the velocity direction is from the node toward the antinodes, where the new vapor bubbles start growing. The vapor flow toward the antinode makes the film surrounding the bubble thinner. The fresh vapor in the thin region, due to pressure difference, is also convected toward the antinode, thus leading to bubble formation and growth. As the film thins, the greater is the superheat, the more vapor is produced, and thus the greater is the strength of the instability because of increased relative velocity between the liquid and vapor region. The instability originating because of the presence of a relative velocity between two layers of fluids is called Kelvin-Helmholtz instability. In the presence of an acceleration from heavier fluid toward lighter fluid, this instability is called Taylor-Helmholtz instability. Fast Fourier transform (FFT) of the space-averaged Nusselt number for water at near critical with a superheat of 10 K shows three distinct frequency peaks (Fig. 20). The frequency domain plot also shows the presence of super harmonics, which can be obtained by $m_1 f_1 + m_2 f_2$, where f_1 is the frequency corresponding to the largest amplitude, f_2 is a subharmonic, and m_1 and m_2 are integers. FFT of the space-averaged Nusselt number for the case of water at near critical condition with a superheat of 15 K (Fig. 21) shows that the subharmonic present in the FFT plot for 10 K superheat has subsided and only the single most dominating peak dictates the time period of the periodic cycle.

A simplified model of film boiling suggested by Panzarella *et al.*[20] was also used to study the initial growth of the film for qualitative understanding and comparisons. Using lubrication approximation, a nondimensionalized equation was derived for the height of the interface "h" given as

$$h_\tau = \frac{Q}{h} - \frac{1}{12}[h^3(h + h_{xx})_x]_x, \tag{32}$$

where Q ($=E\Delta T'_{sup}/B$) is a function of evaporation number $E=k_g\mu_g T_{sat}/[\rho_l(\rho_l-\rho_g)h_{lg}gd^3]$, Bond number $B=[d^2(\rho_l$

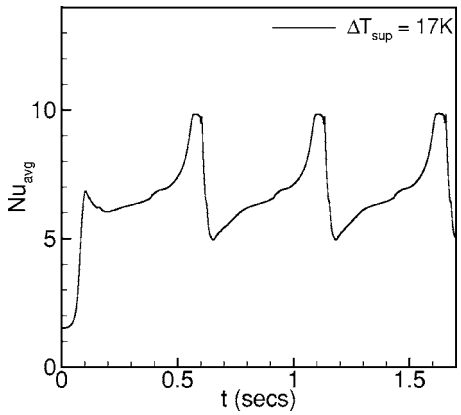

FIG. 19. Space-averaged Nusselt number variation with time for water (P_r=0.99) with ΔT_{sup}=17 K.

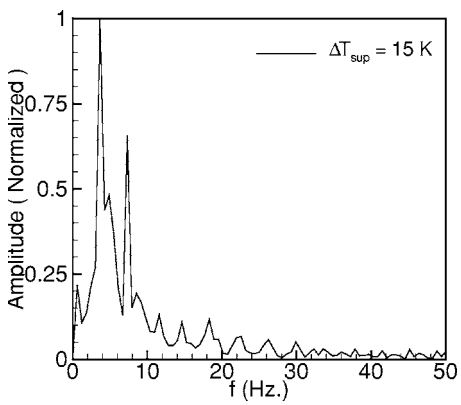

FIG. 21. Normalized FFT of Nusselt number variation with time for water (P_r=0.99) with ΔT_{sup}=15 K.

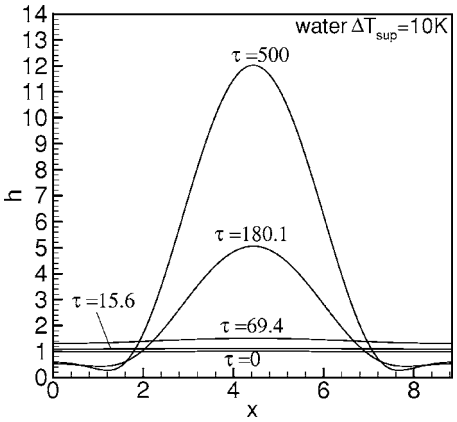

FIG. 22. Interface morphology at different instances for water (P_r=0.99) with ΔT_{sup}=10 K using the lubrication approximation model.

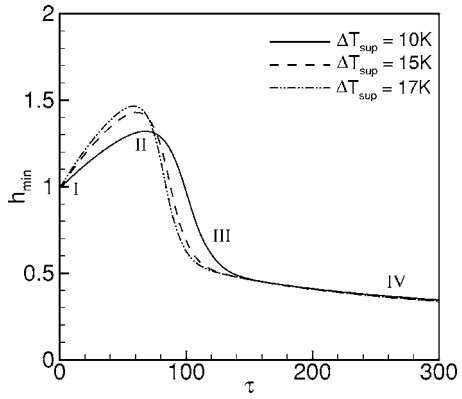

FIG. 24. Comparison of variation in minimum film thickness for water (P_r=0.99) with ΔT_{sup}=10,15, and 17 K.

$-\rho_g)g/\sigma]$, nondimensionalized superheat is $\Delta T'_{sup}$, and d is the average initial thickness. The above partial differential equation was solved by discretizing in x and solving the system of time ordinary differential equations by adaptive size Gear's algorithm for stiff systems. Figure 22 shows the interface morphology obtained for water at near critical pressure (219 bars) at 10 K superheat by solving Eq. (32). As expected, higher superheat produces more vapor per unit time and causes more vapor transport. Figure 23 shows a comparison between profiles for a superheat of 10 and 17 K at the same nondimensional time τ=70 corresponding to the initial growth. The nondimensional time τ is given by $Bt/\{\mu/[gd(\rho_l-\rho_g)]\}$. Interestingly, the minimum thickness of the film (Fig. 24), after attaining a maximum, decreases more rapidly with higher superheats. The minimum thickness falls and asymptotically assumes a stable value. Region I–II in Fig. 24 represents the uniform growth of the vapor film. Between II and III, the crest starts growing rapidly and the interface surrounding the crest (Fig. 23) falls rapidly and attains a stable value (IV), after which the crest continuously grows to form a bubble. The rapid fall in the minimum film thickness for higher superheats reflects the faster dynamics at higher heat fluxes, but as seen in simulations (Secs. I and II), fluctuations are more for lower superheats.

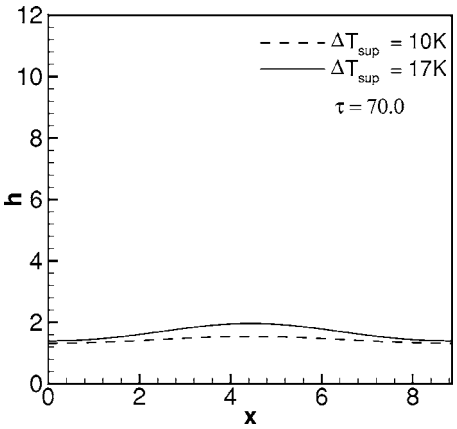

FIG. 23. Comparison of film thickness for water (P_r=0.99) with ΔT_{sup} =10 and 17 K at the nondimensional time τ=70.

Although the lubrication model is rather simplistic and cannot predict the formation of a complete bubble and its detachment, it has been used here to study the characteristics of heat flux during the initial phase of bubble growth in film boiling. The model distinctly shows the bivalent nature of heat flux during the bubble growth. Comparing with the results obtained by simulations, the lubrication model corresponds to the trough region of the Nusselt number profile (Fig. 9). The approach toward the minimum of the space-averaged Nusselt number represents the uniform growth. The rise in the Nusselt number after the minimum corresponds to the dip in the interface surrounding the growing bubble, and the step in the Nusselt number profile represents the point after which the minimum film thickness attains a stable value (region IV in Fig. 24). The Nusselt number profile shows a further increase as the bubble starts to form a neck.

V. CONCLUSIONS

The numerical simulation of bubble growth, based on the CLSVOF technique, provides deep insight into the physics of bubble formation in film boiling. The following are the key conclusions of the study.

(A) A time periodic formation of bubbles occurs alternatively at the nodes and antinodes, which are the two neighboring sites for the bubble nucleation. At near critical pressures, there exists a critical superheat value above which the vapor-jet-like columns form at the nodes. The bubble growth and detachment occurs periodically at the antinodes.

(B) The frequency of bubble detachment is a function of the amount of energy transfer (degree of superheat). Increased superheat increases the frequency of bubble formation. Superheat opposes the instability in the initial growth period of the film, resulting in the uniform growth of the film. But later, it enhances the instability and leads to the bubble formation.

(C) The frequency of bubble detachment is higher in the case of R134a (near critical condition) as compared to water (at near critical condition). The frequency of bubble detachment reduces considerably for the case of R134a at far critical condition.

(D) The increase in superheat increases the frequency of bubble formation but ensures film boiling by preventing the film from rupturing due to the Rayleigh-Taylor instability. With the growth of instability, more regions around the bubble become vapor-deficient and the space-averaged Nusselt number increases. The space-averaged Nusselt number is maximum at the point of detachment of the bubble.

(E) FFT of the space-averaged Nusselt number profile shows two dominant frequency peaks for a superheat of 10 K. At a superheat of 15 K the subharmonic peak subsides, showing the effect of heat flux on the instability.

ACKNOWLEDGMENTS

The research was supported by the MHRD Grant No. MHRD/R&D/20050070. The authors are grateful to Daniel Gerlach of LSTM, University of Erlangen-Nuremberg of Germany, for many useful discussions.

[1] C. W. Hirt and B. D. Nichols, "Volume of fluid (VOF) method for the dynamics of free boundary," J. Comput. Phys. **39**, 201 (1981).
[2] W. F. Noh and P. Woodward, in *SLIC (Simple Line Interface Calculation)*, edited by A. I. van Dooren and P. J. Zandbergen, Lecture Notes in Physics Vol. 59 (Springer, New York, 1976), p. 330.
[3] D. L. Youngs, "Time-dependent multi-material flow with large fluid distortion," in *Numerical Methods for Fluid Dynamics*, edited by K. W. Morton and M. J. Baines (Academic, New York, 1982).
[4] E. G. Puckett, A. S. Almgren, J. B. Bell, D. L. Marcus, and W. J. Rider, "A high-order projection method for tracking fluid interfaces in variable density incompressible flows," J. Comput. Phys. **130**, 269 (1997).
[5] Y. Renardy and M. Renardy, "PROST: A parabolic reconstruction of surface tension for the volume of fluid method," J. Comput. Phys. **183**, 400 (2002).
[6] S. Osher and J. A. Sethian, "Fronts propagating with curvature-dependent speed: Algorithms based on Hamilton-Jacobi formulations," J. Comput. Phys. **79**, 12 (1988).
[7] J. A. Sethian, *Level Set Methods and Fast Marching Methods* (Cambridge University Press, Cambridge, UK, 1999).
[8] A. Bourlioux, "Coupled level-set volume-of-fluid algorithm for tracking material interfaces," Proceedings of the 6th International Symposium on Computational Fluid Dynamics, Lake Tahoe, CA (1995), 15.
[9] M. Sussman and E. G. Puckett, "A coupled level set and volume-of-fluid method for computing 3D and axisymmetric incompressible two-phase flows," J. Comput. Phys. **162**, 301 (2000).
[10] M. Sussman, "A second order coupled level-set and volume-of-fluid method for computing growth and collapse of vapor bubbles," J. Comput. Phys. **180**, 110 (2003).
[11] P. J. Berenson, "Film-boiling heat transfer from a horizontal surface," J. Heat Transfer **83**, 351 (1961).
[12] G. Son and V. K. Dhir, "Numerical simulation of saturated film boiling on a horizontal surface," J. Heat Transfer **119**, 525 (1997).
[13] D. Banerjee and V. K. Dhir, "Study of subcooled film boiling on a horizontal disc: Part I—Analysis," J. Heat Transfer **123**, 271 (2001).
[14] D. Juric and G. Tryggvason, "Computations of boiling flows," Int. J. Multiphase Flow **24**, 387 (1998).
[15] G. Son and V. K. Dhir, "Numerical simulation of film boiling near critical pressure with a level set method," J. Heat Transfer **120**, 183 (1998).
[16] M. Reimann and U. Grigull, "Warmeubergang bei freier Konvektion und Filmsieswn im kritischen Gebiet von Wasser und Kohlendioxid," Waerme-Stoffuebertrag. **8**, 229 (1975).
[17] S. W. J. Welch and J. Wilson, "A volume of fluid based method for fluid flows with phase change," J. Comput. Phys. **160**, 662 (2000).
[18] S. W. J. Welch and T. Rachidi, "Numerical simulation of film boiling including conjugate heat transfer," Numer. Heat Transfer, Part B **42**, 35 (2002).
[19] D. K. Agarwal, S. W. J. Welch, G. Biswas, and F. Durst, "Planar simulation of bubble growth in film boiling in near-critical water using a variant of the VOF method," J. Heat Transfer **126**, 1 (2004).
[20] C. H. Panzarella, S. H. Davis, and S. G. Bankoff, "Nonlinear dynamics in horizontal film boiling," J. Fluid Mech. **402**, 163 (2000).
[21] J. U. Brackbill, D. B. Kothe, and C. Zemach, "A continuum method for modeling surface tension," J. Comput. Phys. **100**, 335 (1992).
[22] Y. C. Chang, T. Y. Hou, B. Merriman, and S. Osher, "A level set formulation of Eulerian interface capturing methods for incompressible fluid flows," J. Comput. Phys. **124**, 449 (1996).
[23] M. Rudman, "Volume-tracking methods for interfacial flow calculations," Int. J. Numer. Methods Fluids **24**, 671 (1997).
[24] D. Gerlach, G. Tomar, G. Biswas, and F. Durst, "Comparison of volume-of-fluid methods for surface tension-dominant two-phase flows," Int. J. Heat Mass Transfer (to be published).
[25] S. Popinet and S. Zaleski, "A front-tracking algorithm for accurate representation of surface tension," Int. J. Numer. Methods Fluids **30**, 775 (1999).
[26] A. Prosperetti, "Motion of two superimposed viscous fluids," Phys. Fluids **24**, 1217 (1981).
[27] S. Chansrashekhar, *Hydrodynamic and Hydromagnetic Stability* (Dover, New York, 1981).
[28] J. P. Burelbach, S. G. Bankoff, and S. H. Davis, "Nonlinear stability of evaporating/condensing liquid films," J. Fluid Mech. **195**, 463 (1988).